




Core@shell structured $Ti_3C_2T_x@Ni$ -reinforced Al composites with enhanced mechanical properties and electromagnetic interference shielding performance

Xiachen Fan¹, Shibo Li^{1,*} , Weimin Xu¹, Jie Hu¹, Shujun Hu¹, Wenbo Yu¹, and Yang Zhou¹

¹ School of Mechanical and Electronic Control Engineering, Beijing Jiaotong University, Beijing 100044, China

Received: 8 February 2021

Accepted: 9 May 2021

Published online:
17 May 2021

© The Author(s), under exclusive licence to Springer Science+Business Media, LLC, part of Springer Nature 2021

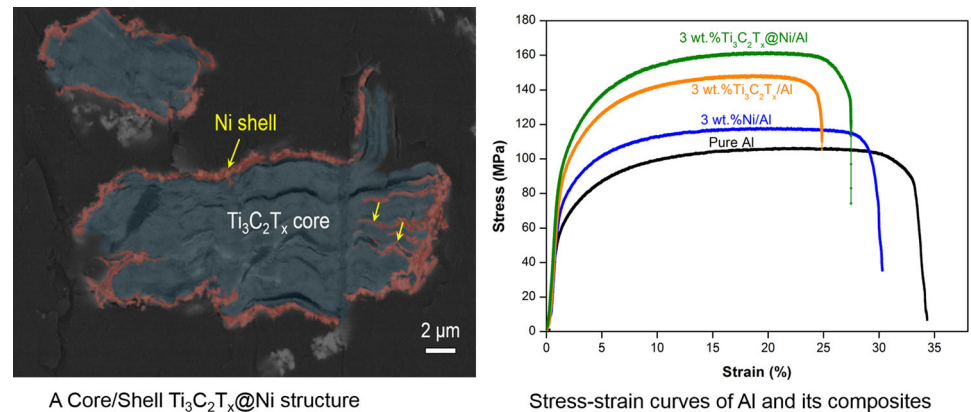
ABSTRACT

Al matrix composites reinforced with core@shell structured $Ti_3C_2T_x@Ni$ particles have been prepared by pressureless-sintering and hot-extrusion technology. The as-prepared 1–3 wt% $Ti_3C_2T_x@Ni/Al$ composites demonstrated improved mechanical properties and electromagnetic interference shielding effectiveness (EMI SE). The Vickers hardness and tensile strength of $Ti_3C_2T_x@Ni/Al$ composites increased with increasing reinforcement content. A hardness of 0.36 GPa and a tensile strength of 163 MPa were achieved in the 3 wt% $Ti_3C_2T_x@Ni/Al$ composite, increased by 33% and 66%, respectively, but the ductility did not compromise too much, as compared with pure Al. The main mechanisms for the enhanced tensile strength but the maintained plasticity of the composites are the homogeneous distribution of reinforcement $Ti_3C_2T_x@Ni$ particles, the efficient transfer of the applied stress from the soft Al matrix to the reinforcing particles, and the multi-absorbing energy mechanisms: delamination, buckling and kinking of $Ti_3C_2T_x$ particles, crack branching and crack deflection. The 3 wt% $Ti_3C_2T_x@Ni/Al$ composite also exhibited an enhanced EMI SE performance due to the synergic effect of the absorption loss of the $Ti_3C_2T_x$ core and the magnetic loss of the Ni shell.

Handling Editor: N. Ravishankar.

Address correspondence to E-mail: shbli1@bjtu.edu.cn

GRAPHICAL ABSTRACT



Introduction

Ti₃C₂T_x is one of the most attractive materials in a two-dimensional (2D) MXene family [1, 2]. Ti₃C₂T_x is produced by wet chemical etching of Ti₃AlC₂ precursor. Ti₃C₂T_x surfaces are always decorated with abundant surface functional groups including -F, -OH, -O and/or -Cl (T_x represents the surface functional groups). Ti₃C₂T_x has a combination of physical, mechanical and functional properties, and exhibits a wide range of applications for energy storage, electromagnetic interference shielding, water purification, sensor, and lubrication [3–6]. Recently, Ti₃C₂T_x has been demonstrated as an effective reinforcement to improve the performance of polymer, metal and ceramic matrix composites due to the good interfacial bonding between reinforcement and matrix [7–12]. Ti₃C₂T_x has metallic characterization and rich surface functional groups which improve the wettability of Ti₃C₂T_x with polymer, metal and ceramic matrices. The good wettability of Ti₃C₂T_x with matrices endows the composites with strong bonding interfaces, thus leading to effective load transfer from the matrix to the reinforcement. For example, surface functional groups permit Ti₃C₂T_x to create covalent bonds with polymer matrix to ensure strong interfacial adhesion and good stress transfer across the interfaces [7, 8]. Ti₃C₂T_x/Al composites demonstrate improved hardness and tensile strength with increasing Ti₃C₂T_x content from 0.5 to 3 wt%; 92%

and 50% improvements in hardness and strength are, respectively, achieved in the 3 wt% Ti₃C₂T_x/Al composite [9]. A 43% improvement of tensile strength over pure Cu can be obtained in a 5 vol% Ti₃C₂T_x/Cu composite [10]. Ti₃C₂T_x as an attractive reinforcement incorporated in metal matrices avoids problems appeared in graphene- and CNTs-reinforced composites, such as agglomeration, weak bonding interfaces and interfacial reactions [13, 14].

Recently, core@shell structured particles-reinforced composites have attracted considerable attention due to their enhanced performance and combined functional properties [15–18]. A core@shell structured particle consists of a core (inner material) and a shell (outer layer material), possessing distinct advantages as compared with its single component. The incorporation of core@shell structured reinforcements in Al composites demonstrates improved either strength or ductility [19–23]. Al matrix composites reinforced with specially designed core@shell particles have achieved a higher ductility while retaining the tensile strength [19], or a higher strength but maintaining the ductility [21, 22], overcoming the trade-off between strength and ductility. The main mechanisms for the improved mechanical properties are attributed to (1) the uniform distribution of core@shell structured particles, (2) the strong bonding interfaces formed between the shell and Al matrix, withstanding the applied stress transferred from Al matrix, and (3) crack deflection in the

core@shell structure and crack blunt by the soft core, dissipating the crack propagation energy.

Our previous work showed that $Ti_3C_2T_x$ -reinforced Al composites have a homogeneous microstructure and strong bonding interfaces, resulting in higher tensile strength and hardness but lower ductility as compared the pure Al material [9]. In the present study, the core@shell structured $Ti_3C_2T_x@Ni$ particles were incorporated in Al matrix to further improve its strength but maintain its ductility. In addition, electromagnetic interference shielding properties of $Ti_3C_2T_x@Ni$ -Al composites were also investigated. X-ray diffraction analysis, scanning electron microscopy, and transmission electron microscopy techniques were used to characterize the as-prepared composites.

Material and methods

Preparation of $Ti_3C_2T_x$

$Ti_3C_2T_x$ was prepared by selective etching of precursor Ti_3AlC_2 in a 40% HF solution at 50 °C for 0.5 h. The detailed processing has been described in elsewhere [24].

Preparation of core@shell structured $Ti_3C_2T_x@Ni$

To prepare core@shell structured $Ti_3C_2T_x@Ni$ particles, electroless Ni plating was adopted. Firstly, the $Ti_3C_2T_x$ powder was subjected to the treatment of activation and sensitization. One gram of $Ti_3C_2T_x$ powder was added to 40 ml of sensitization and activation solution containing 3.2 ml of 36% HCl, 16 g/L of $SnCl_2 \cdot 2H_2O$, 0.4 g/L of $PdCl_2$ and 160 g/L of NaCl, and then mixed in a magnetic stirring device at room temperature for 1 h. The solution was centrifugally separated at 4000 rpm and then washed with deionized water until the pH of the liquid was about 6.5–7. The activated powder was immersed in a HCl solution and stirred for 10 min, and then washed with deionized water and vacuum dried at 50 °C for 24 h. Secondly, the electroless Ni plating process was performed. 0.25 of the activated and sensitized $Ti_3C_2T_x$ powder was immersed in 250 ml of plating solution containing 20 g/L of $NiSO_4 \cdot 6H_2O$, 62.5 g/L of $N_2H_4 \cdot H_2O$, 6.25 g/L of EDTA-2Na, and 6.25 g/L of $C_6H_6Na_2O_7$. The solution was stirred in the

magnetic stirring device at 90 °C for about 15 min. The pH was kept at 12 by using a 250 g/L of NaOH solution. The Ni-coated powder was washed and then dried.

Preparation of $Ti_3C_2T_x@Ni$ -Al composites

$Ti_3C_2T_x@Ni$ powder was mixed with pure Al powder (particle size –300 mesh, 99.5% purity) for 10 h. The content of $Ti_3C_2T_x@Ni$ powder was 1 wt%, 2 wt%, and 3 wt% in the mixture to prepare 1 wt%, 2 wt%, and 3 wt% $Ti_3C_2T_x@Ni/Al$ composites, respectively.

The mixtures were cold-pressed with a pressure of 80 MPa in a steel mold for 5 min to get green compacts with a size of $\Phi 20 \times 15$ mm. The compacts were pressureless-sintered in a furnace at 650 °C for 1 h in Ar. The sintered samples were then hot-extruded at 450 °C with a speed of 5 mm/min. The extrusion ratio was 10:1 (the ratio of cross-sectional areas before and after hot extrusion). The extruded samples have a cross section of 3×10 mm². For comparison, pure Al, $Ti_3C_2T_x/Al$, and Ni/Al samples were also prepared under the same conditions as for $Ti_3C_2T_x@Ni/Al$.

Property measurement

The prepared samples were machined with a wire electrical discharge into specimens for tensile test. The detailed information has been described in elsewhere [9]. Tensile testing was conducted in a WDW-100E test machine with a speed of 0.2 mm/min. Three bars were tested to determine an average value of tensile strength.

The Vickers hardness was measured in a TH700 hardness tester. The hardness indentations were operated at a load of 5 kg and a dwell time of 15 s. Six measurements in different areas were taken under the same load to obtain an average value of hardness.

Electromagnetic interference shielding (EMIS) performance was determined in an Agilent E5071C vector network analyzer in the range of 2–18 GHz. Dimensions of ring-like samples for EMIS performance test are 3.04 mm of inner diameter and 7.0 mm of outer diameter, and 2 mm of thickness.

Characterization

Core@shell structured powder and prepared composites were characterized with X-ray diffraction (XRD) analysis using a D/Max 2200 PC diffractometer (Rigaku Co. Ltd., Tokyo, Japan) applying monochromatic Cu K radiation, scanning electron microscopy (SEM, ZEISS EVO 18, Carl Zeiss SMT, Germany) equipped with an energy-dispersive spectrometer system (EDS), and transmission electron microscopy (TEM, JEM-2100F (JEOL Ltd., Tokyo, Japan) with an operating voltage of 200 kV.

Results and discussion

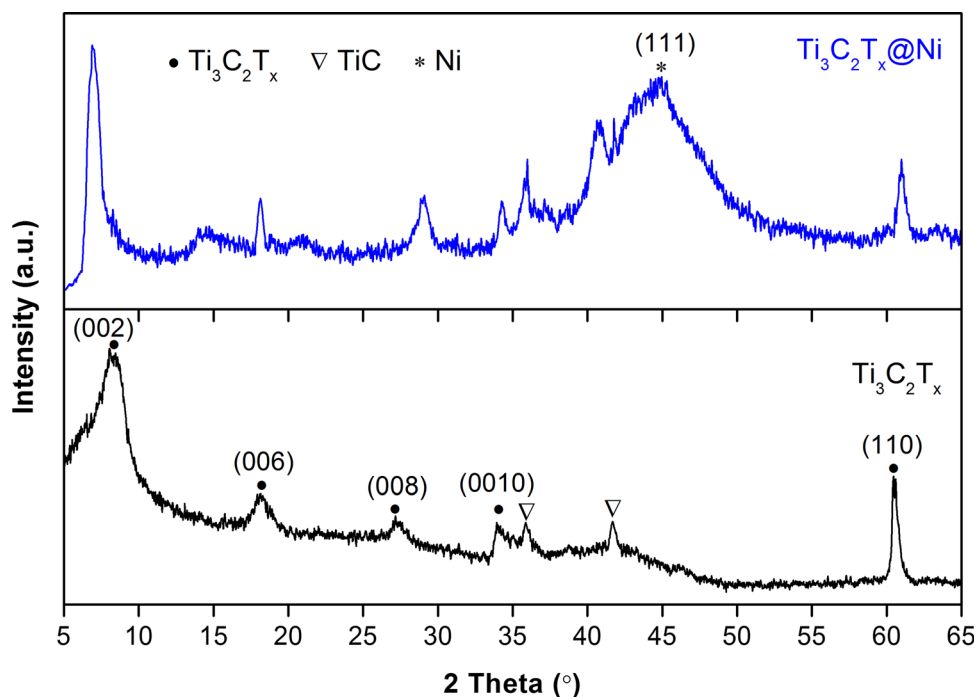
Characterization of powder and composites

Figure 1 shows the XRD patterns of $\text{Ti}_3\text{C}_2\text{T}_x$ and $\text{Ti}_3\text{C}_2\text{T}_x@\text{Ni}$ powders. For the $\text{Ti}_3\text{C}_2\text{T}_x$ powder, broaden peaks belonging to $\text{Ti}_3\text{C}_2\text{T}_x$ and two weak peaks belonging to TiC were detected in the XRD pattern. A small amount of TiC may be introduced from the precursor Ti_3AlC_2 powder. After electroless Ni plating, a broad peak at about 45° belonging to Ni appeared in the XRD pattern, indicating the formation of the nano-sized Ni particles. In addition, Ni plating induced the shift of (002) peak for $\text{Ti}_3\text{C}_2\text{T}_x$ from 8.28 to 6.88° , suggesting that Ni atoms diffused

into interlayer spacing of $\text{Ti}_3\text{C}_2\text{T}_x$ and led to the expansion of spacing distance, from 0.999 to 1.201 nm.

SEM micrographs demonstrate the morphologies of $\text{Ti}_3\text{C}_2\text{T}_x$ and $\text{Ti}_3\text{C}_2\text{T}_x@\text{Ni}$ (Fig. 2). The $\text{Ti}_3\text{C}_2\text{T}_x$ particles show a distinctive feature with multiple stacking nanolayers (Fig. 2a), induced by the selective etching of Al atomic layers from Ti_3AlC_2 precursor. After Ni plating, the surfaces of $\text{Ti}_3\text{C}_2\text{T}_x$ were covered with Ni particles (Fig. 2b). These Ni particles are round in shape with a nano-sized dimension. Figure 2c is a backscattered SEM micrograph showing the cross section of a core@shell structured $\text{Ti}_3\text{C}_2\text{T}_x@\text{Ni}$ particle. A Ni layer is less than $0.5 \mu\text{m}$ in thickness covering the $\text{Ti}_3\text{C}_2\text{T}_x$ core particle (Fig. 2b). It should be noted that the multiple inner layers of $\text{Ti}_3\text{C}_2\text{T}_x$ were also plated with Ni (marked by arrows), but the inner Ni layers are thinner than the outer layer, indicating that the formation of Ni layer is controlled by the diffusion, and the nucleation and growth of Ni is prefer to occur on the outer surfaces of $\text{Ti}_3\text{C}_2\text{T}_x$. The EDS analysis reveals the elemental Ti and Ni distributions in the $\text{Ti}_3\text{C}_2\text{T}_x@\text{Ni}$ particles (Fig. 2d). It can be found the distribution of Ni on the surface and in the inner of $\text{Ti}_3\text{C}_2\text{T}_x$, forming a multiple-coated $\text{Ti}_3\text{C}_2\text{T}_x@\text{Ni}$ structure. Such a structure may deflect the crack propagation paths and blunt the crack tips as cracks entered into the reinforcing

Figure 1 XRD patterns of **a** $\text{Ti}_3\text{C}_2\text{T}_x$ and **b** Core@shell structured $\text{Ti}_3\text{C}_2\text{T}_x/\text{Ni}$.



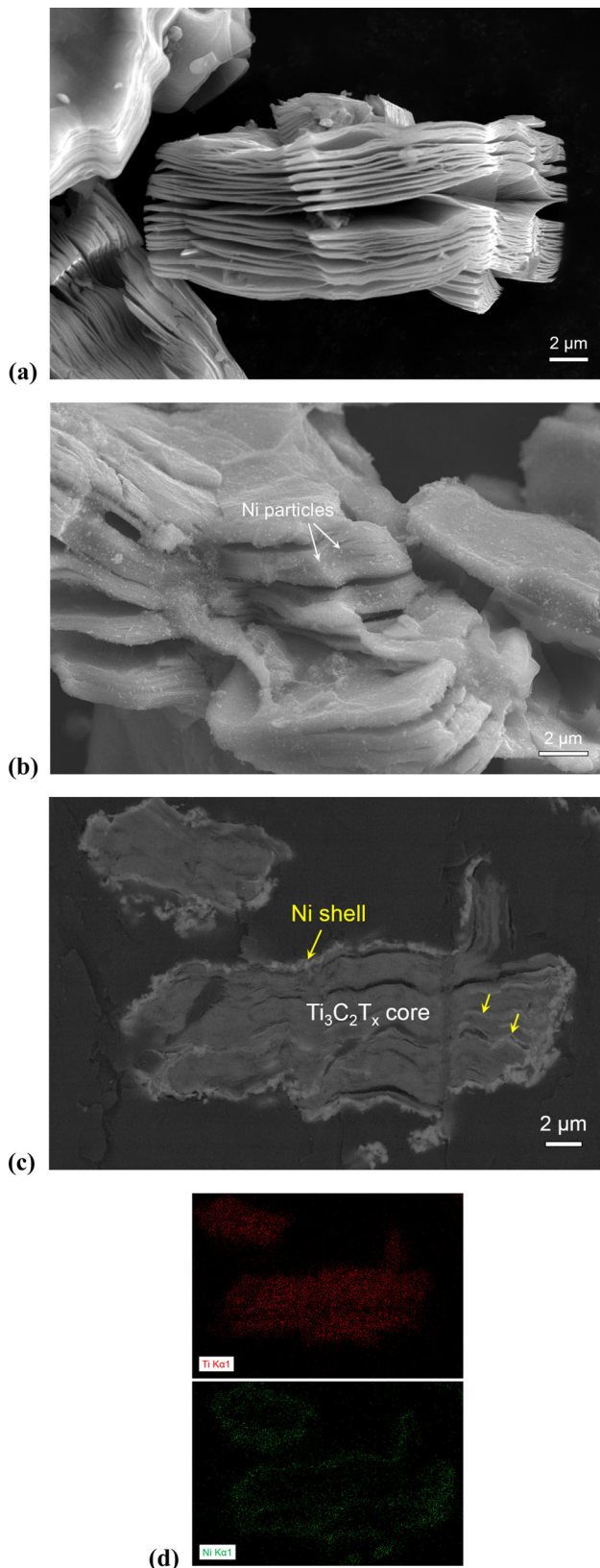


Figure 2 SEM micrographs of **a** $\text{Ti}_3\text{C}_2\text{T}_x$, **b** a Ni-coated $\text{Ti}_3\text{C}_2\text{T}_x$ particle, and **c** a cross-sectional back-scattered second electron (BSE) image of Ni-coated $\text{Ti}_3\text{C}_2\text{T}_x$ particles, showing a core@shell structure. **d** EDS maps of Ti and Ni elemental distributions.

particles, contributing to the improvement of mechanical properties of composites.

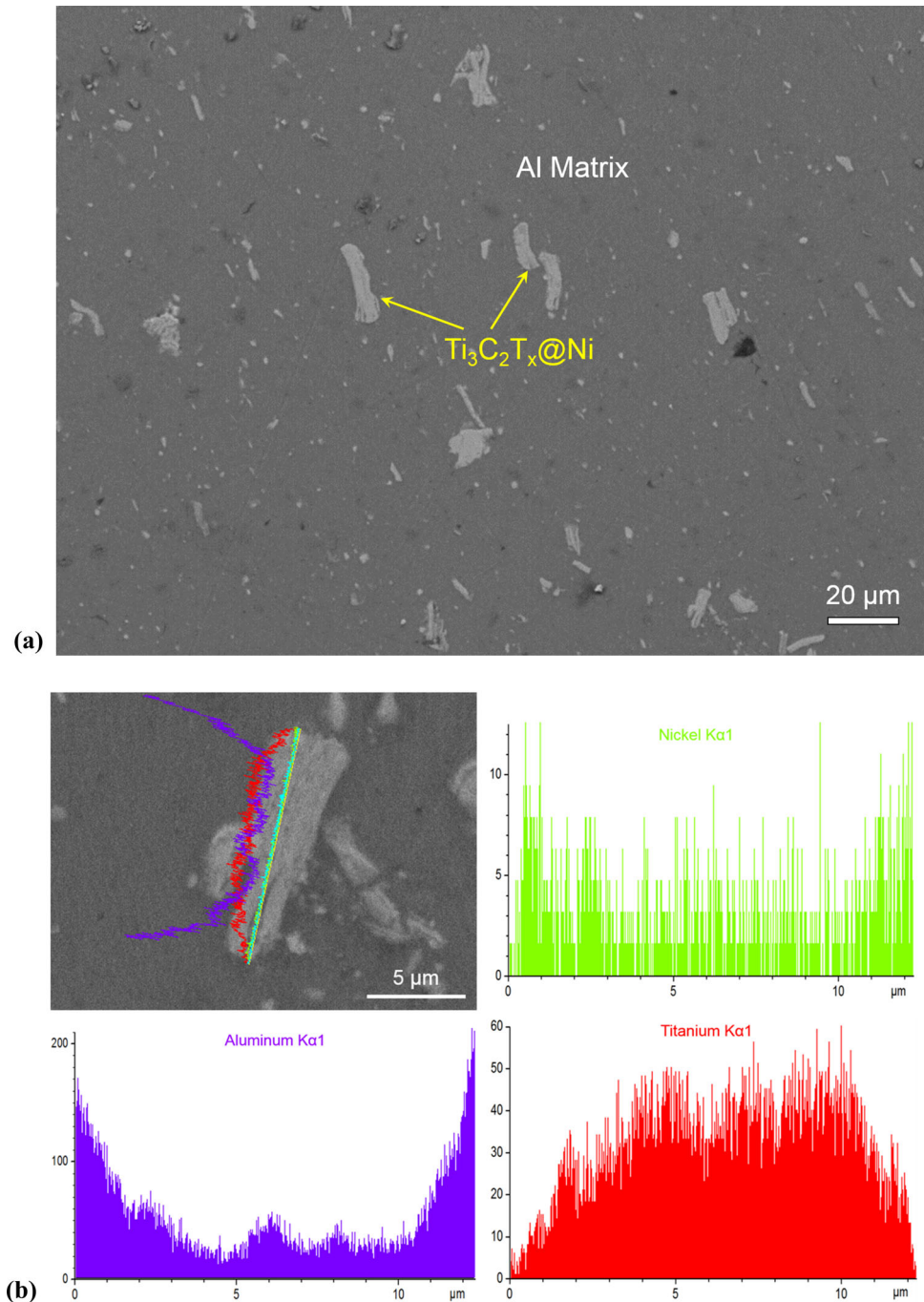
The as-prepared 3 wt% $\text{Ti}_3\text{C}_2\text{T}_x@Ni/Al$ composite shows a homogenous distribution of reinforcement (Fig. 3a). No agglomerated $\text{Ti}_3\text{C}_2\text{T}_x@Ni$ particles were detected. The uniform microstructure contributes to the improved mechanical properties. The EDS line analysis reveals the distribution of Ni almost on the surface of $\text{Ti}_3\text{C}_2\text{T}_x$ (Fig. 3b). Al signals were also detected in the $\text{Ti}_3\text{C}_2\text{T}_x$, indicating that Al atoms diffuse into the opening space in the layered $\text{Ti}_3\text{C}_2\text{T}_x$ to form Al thinner layers (Fig. 3b).

Mechanical properties

Figure 4a shows the Vickers hardness as a function of reinforcement content in the $\text{Ti}_3\text{C}_2\text{T}_x@Ni/Al$ composites, together with Ni/Al and $\text{Ti}_3\text{C}_2\text{T}_x/Al$ composites for comparison. For Ni/Al and $\text{Ti}_3\text{C}_2\text{T}_x/Al$ composites, their hardness values increased with increasing reinforcement. It can be found that the hardness of Ni/Al composites is lower than that of $\text{Ti}_3\text{C}_2\text{T}_x/Al$ composites, which should be ascribed to the soft Ni particles as compared with hard $\text{Ti}_3\text{C}_2\text{T}_x$ particles. For $\text{Ti}_3\text{C}_2\text{T}_x@Ni/Al$ composite, it has a hardness comparable to $\text{Ti}_3\text{C}_2\text{T}_x/Al$ composite with the same reinforcement content of 1 wt%. As the reinforcement content exceeded 1 wt%, the hardness values of $\text{Ti}_3\text{C}_2\text{T}_x@Ni/Al$ are lower than those of $\text{Ti}_3\text{C}_2\text{T}_x/Al$ composites. The decreased hardness in $\text{Ti}_3\text{C}_2\text{T}_x@Ni/Al$ composites may be caused by the introduction of Ni metallic element with a hardness lower than $\text{Ti}_3\text{C}_2\text{T}_x$. In addition, the density of Ni (8.9 g/cm³) is higher than about 4.3 g/cm³ [25] for $\text{Ti}_3\text{C}_2\text{T}_x$. Hence, the real content of $\text{Ti}_3\text{C}_2\text{T}_x$ hard particles in 3 wt% $\text{Ti}_3\text{C}_2\text{T}_x@Ni/Al$ composite is lower than that in 3 wt% $\text{Ti}_3\text{C}_2\text{T}_x/Al$ composite, inducing the decrease in hardness.

Figure 4b demonstrates the relationship between tensile strength and reinforcement content for three kinds of composites. The tensile strengths of composites all increased with increasing reinforcement content. $\text{Ti}_3\text{C}_2\text{T}_x@Ni/Al$ composites and $\text{Ti}_3\text{C}_2\text{T}_x/Al$

Figure 3 Back-scattered SEM micrographs of the polished surface of 3 wt% $Ti_3C_2T_x$ /Ni–Al composite. **a** A low BSE image, and **b** EDS line analysis showing the distributions of Ti, Ni and Al.



composites both exhibit increased tensile strength as compared with pure Al, but the former composites are higher than the latter composites in tensile strength. In the $Ti_3C_2T_x$ /Al composites, the strengthening mechanisms including the homogeneous distribution of $Ti_3C_2T_x$, strong bonding interfaces between $Ti_3C_2T_x$ and Al, and phase boundaries pinning dislocation movement endow the composites with improved mechanical properties [9]. However,

in the $Ti_3C_2T_x@Ni$ /Al composites, except for the above mentioned strengthening mechanisms, nano-sized grain or phase boundaries contribute to the improvement of strength. Grain size/boundary is one of the predominant strengthening mechanisms [26]. For example, a thinner Ni shell in the $Ti_3C_2T_x@Ni$ particles is composed of many Ni nano grains, accompanying with numerous grain boundaries. A large number of nano-sized Ni grain boundaries, Ni/

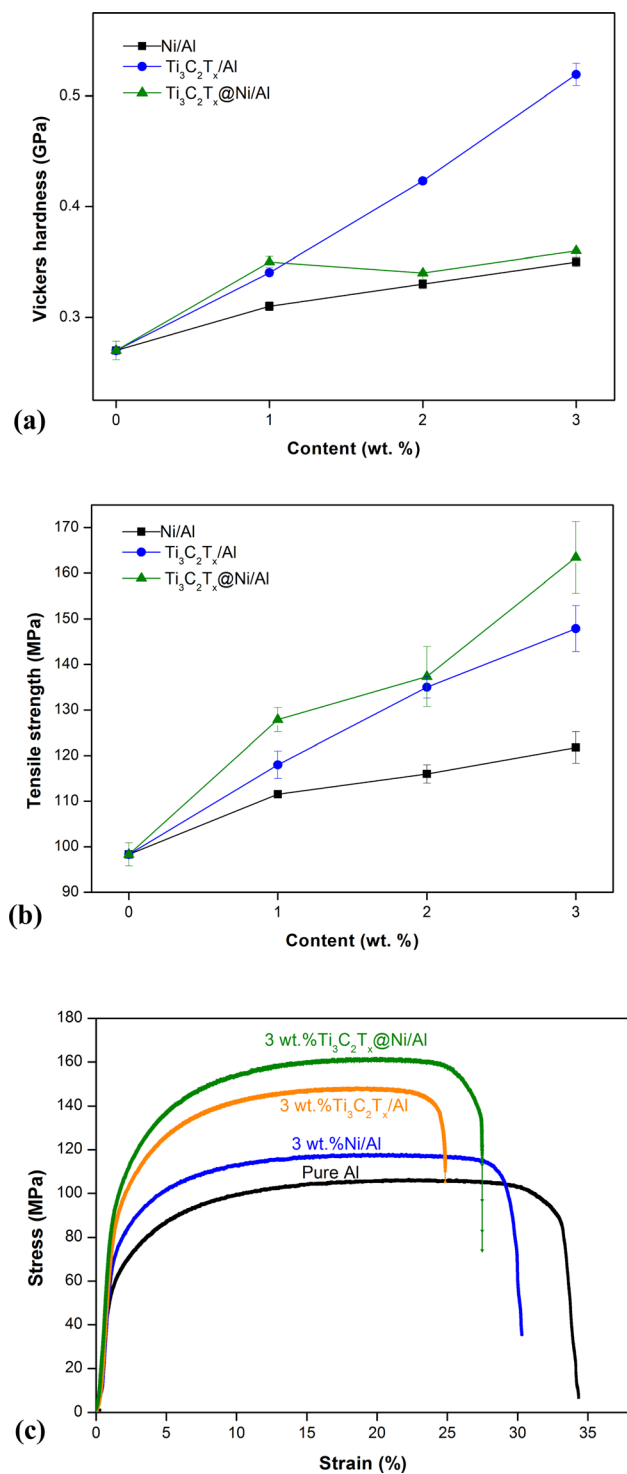


Figure 4 Mechanical properties of Ti₃C₂T_x/Ni–Al, together with Ti₃C₂T_x/Al and Ni/Al composites for comparison. **a** Vickers hardness and **b** Tensile strength as a function of reinforcement content, **c** Comparison of stress–strain curves of pure Al, 3 wt% Ni/Al, 3 wt% Ti₃C₂T_x/Al and 3 wt% Ti₃C₂T_x@Ni/Al materials.

Al and Ni/Ti₃C₂T_x phase boundaries impede the movement of dislocations during tensile deformation, synergistically contributing the increased tensile strength. The Ti₃C₂T_x@Ni/Al composites having the highest tensile strength among the three kinds of composites further confirm the positive reinforcing effect of the core@shell structured particles in Al matrix composites. The highest tensile strength of 163 MPa for 3 wt% Ti₃C₂T_x@Ni/Al composite was achieved. The increment of tensile strength is up to 66% as compared with the pure Al material.

Generally, the increase in the tensile strength is at a sacrifice of ductility. Therefore, the engineering stress–strain curves of 3 wt% Ti₃C₂T_x@Ni/Al, 3 wt% Ti₃C₂T_x/Al, 3 wt% Ni/Al and pure Al were compared in the present study (Fig. 4c). According to the stress–strain curve, it can be found that both of the yield strength and tensile strength for 3 wt% Ti₃C₂T_x@Ni/Al and 3 wt% Ti₃C₂T_x/Al composite are higher than those of other two materials. It should be noted that the ductility of 3 wt% Ti₃C₂T_x@Ni/Al is slightly lower than that of pure Al, but larger than that of 3 wt% Ti₃C₂T_x/Al. The elongations are 27% and 34%, respectively, for 3 wt% Ti₃C₂T_x@Ni/Al and pure Al. Therefore, the 3 wt% Ti₃C₂T_x@Ni/Al composite exhibited improved tensile strength but with the maintained plasticity, due to the contribution of the core@shell structure.

Figure 5 demonstrates the fracture surface of the 3 wt% Ti₃C₂T_x@Ni/Al composite. The fracture surface shows a ductile fracture mode, with many dimples in the Al matrix (Fig. 5a). Some Ti₃C₂T_x@Ni particles were pulled out from the matrix (marked with arrows in Fig. 5a). Some pores may be formed by plastic deformation or induced by the pull-out of reinforcing particles. A high magnification SEM image clearly presents the good bonding of Ti₃C₂T_x particles with the Al matrix (Fig. 5b). On the surface of the sample after tensile test, a deformed Ti₃C₂T_x particle exhibits a typical feature of delamination, buckling and kinking (Fig. 5c), similar to the deformed MAX grains [27–29]. In addition, crack branching and deflection in the inner layers of Ti₃C₂T_x are also observed (Fig. 5d). The multi-absorbing energy mechanisms can dissipate the deformation energy and contribute to the increase in strength and ductility of Ti₃C₂T_x@Ni/Al composites.

Figure 6 shows TEM images of 3 wt% Ti₃C₂T_x@Ni/Al composite. No microcracks were found at Ti₃C₂T_x/Al interfaces, suggesting the good interfacial

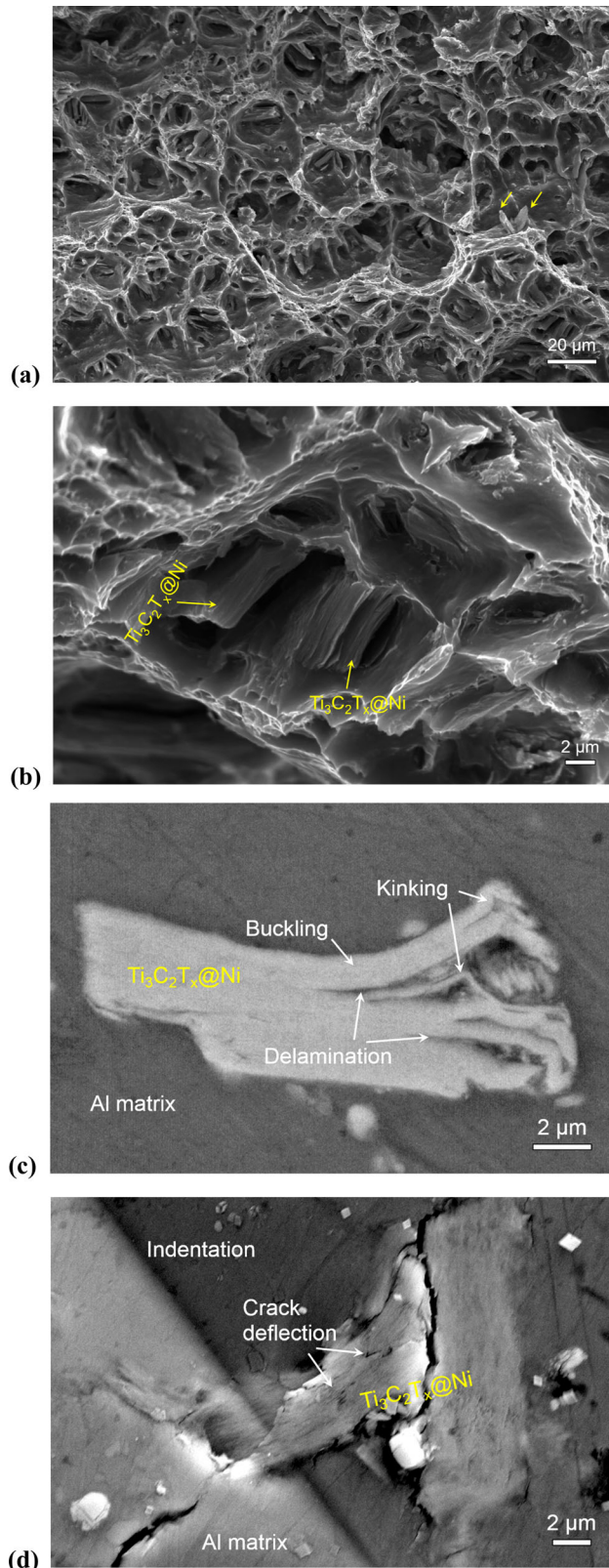


Figure 5 a A low magnification SEM micrograph of fracture surface of 3 wt % $\text{Ti}_3\text{C}_2\text{T}_x/\text{Ni}$ -Al composite after tensile test, b A high magnification SEM micrograph taken from (a), c A SEM micrograph showing the deformed $\text{Ti}_3\text{C}_2\text{T}_x$ after tensile test, d Crack deflection in the $\text{Ti}_3\text{C}_2\text{T}_x$ around the indentation.

adhesion between $\text{Ti}_3\text{C}_2\text{T}_x$ and Al (Fig. 6a). This feature is beneficial to the effective stress transfer from soft Al to the relatively hard reinforcement. In addition, no reaction layers or compounds were detected between Ni, $\text{Ti}_3\text{C}_2\text{T}_x$ and Al. Figure 6b presents a high-resolution TEM image. The measured interplanar spacing is about 1.092 nm corresponding to the (002) plane of $\text{Ti}_3\text{C}_2\text{T}_x$, and about 0.144 nm belonging to the (110) plane of Al. The interplanar spacing of 1.092 nm for $\text{Ti}_3\text{C}_2\text{T}_x$ in the Al matrix is slightly lower than the value of 1.201 nm for the original $\text{Ti}_3\text{C}_2\text{T}_x@\text{Ni}$ particles calculated according to the XRD pattern shown in Fig. 1, which should be ascribed to the fact that the crystal spacing of $\text{Ti}_3\text{C}_2\text{T}_x$ is contracted by the removal of the adsorbed interlayer water and functional groups at processing temperature of 650 °C. A large number of dislocations move toward and accumulate at the phase boundaries of $\text{Ti}_3\text{C}_2\text{T}_x$ and Al (Fig. 6c). The motion of dislocations contributes to the plastic deformation of Al matrix. Also the phase boundaries play an effective role in pinning the motion of dislocations to improve the mechanical properties.

On the basis of the above results, the reasons for the improvements in strength, but the maintainment in the plasticity have been explained as follows: First, the homogeneous distribution of reinforcement particles and the formation of strong interfacial bonding in the Al matrix improves the mechanical properties. Second, the $\text{Ti}_3\text{C}_2\text{T}_x@\text{Ni}$ reinforcing particles impede the motion of dislocations due to a large number of nano-sized grain and phase boundaries during tensile plastic deformation. Third, stresses are effectively transferred from the soft Al metal matrix to $\text{Ti}_3\text{C}_2\text{T}_x@\text{Ni}$ particles, which has been evidenced by the ductile fracture surface with dimples and pulled out $\text{Ti}_3\text{C}_2\text{T}_x@\text{Ni}$ particles. Fourth, as propagating cracks meet the $\text{Ti}_3\text{C}_2\text{T}_x@\text{Ni}$ particles, the propagation paths of cracks are continually deflected in the multiple layers of $\text{Ti}_3\text{C}_2\text{T}_x$, and more energy of propagating cracks is consumed, contributing to the maintained plasticity of composites. Last, the delamination, buckling and kinking of $\text{Ti}_3\text{C}_2\text{T}_x$ can dissipate the

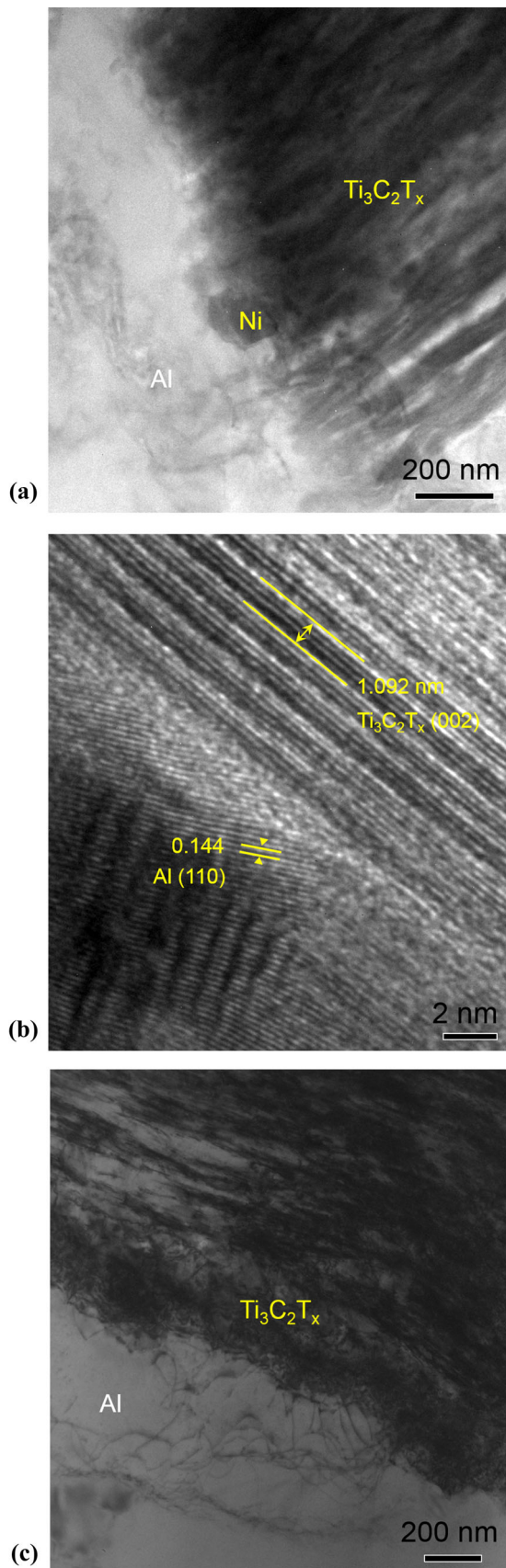


Figure 6 TEM micrographs of 3 wt % $\text{Ti}_3\text{C}_2\text{T}_x/\text{Ni}-\text{Al}$ composite. **a** A low magnification image, **b** A high-resolution TEM, and **c** Dislocations pinned at phase boundaries of $\text{Al}/\text{Ti}_3\text{C}_2\text{T}_x$.

deformation energy and contributes to the increase in strength and ductility of $\text{Ti}_3\text{C}_2\text{T}_x@/\text{Ni}/\text{Al}$ composites.

EMI shielding performance

Generally, there are three basic electromagnetic interference (EMI) shielding mechanisms: Reflection loss (R), Absorption loss (A), and Multiple reflection loss (M). The capability of EMI shielding materials is measured in terms of Shielding effectiveness (SE) value in decibels [dB]. The total EMI SE (SE_T) is the Sum of reflection (SE_R), Absorption (SE_A) and Multiple reflections (SE_M).

For the MXene materials with a multilayer EMI shield, the contribution of internal multiple reflections is combined in the absorption due to the fact that the re-reflected waves are absorbed or dissipated in the form of heat in the shielding material [30].

The total SE_T is described as:

SE_R and SE_A can be calculated based on the scattering parameters (S -parameters) obtained from the vector network analyzer as follows:

$$SE_R = 10 \lg \frac{1}{1 - |S_{11}|^2} \quad (2)$$

$$SE_A = 10 \lg \frac{1 - |S_{11}|^2}{|S_{12}|^2} \quad (3)$$

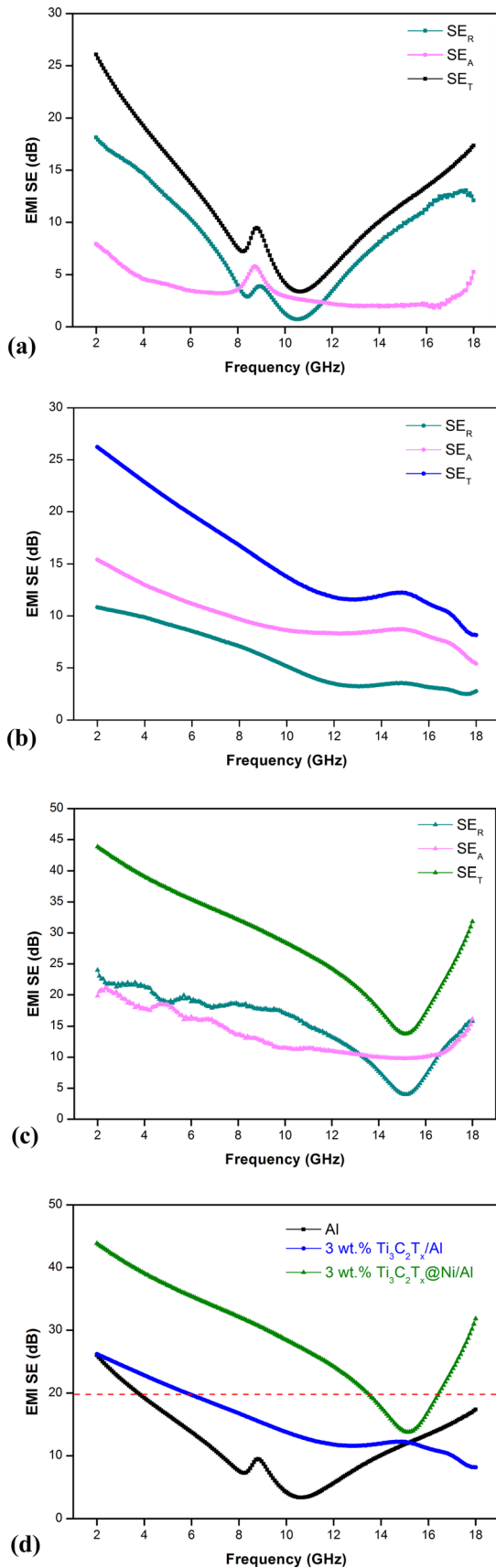
where S_{11} represents the power reflected from port 1 to port 1, and S_{12} represents the power transferred from port 1 to port 2.

Figure 7 shows the SE_T , SE_R and SE_A curves of pure Al, 3 wt% $\text{Ti}_3\text{C}_2\text{T}_x/\text{Al}$ and 3 wt% $\text{Ti}_3\text{C}_2\text{T}_x@/\text{Ni}/\text{Al}$ materials. Al alloys have good EMI SE at frequencies less than 1.5 GHz, and their EMI SE decreases with increasing frequency [31]. The shape of SE curves for samples with the certain thickness is influenced by frequency and electrical conductivity according to Eq. (3):

$$SE = 50 + 10 \log \frac{\sigma}{f} + 1.7t\sqrt{\sigma f} \quad (4)$$

where, σ is the electrical conductivity, f is the frequency, and t is the thickness of shield.

There is little information on the EMI SE of Al in the frequency 2–18 GHz. Figure 7a depicts the SE_T ,



◀ **Figure 7** SE_T, SE_A, and SE_R in the frequency range 2–18 GHz for **a** pure Al, **b** 3 wt% Ti₃C₂T_x/Al and **c** 3 wt% Ti₃C₂T_x@Ni/Al. **d** Comparison of EMI SE for pure Al, 3 wt% Ti₃C₂T_x/Al and 3 wt% Ti₃C₂T_x@Ni/Al composites.

SE_R and SE_A of pure Al. The values of SE_A for Al are less than 10 dB, and are lower than those of SE_R in the frequency before 8 GHz and after 12 GHz. The SE_R curve exhibits a tendency to first decrease and then increase with increasing frequency. The SE_T curve has the same tendency as the SE_R curve, indicating that the reflection loss is the predominant mechanism in the electromagnetic interference shielding due to the high electrical conductivity of Al. The SE_T values of pure Al are lower than 26 dB in the frequency 2–18 GHz.

For 3 wt% Ti₃C₂T_x/Al composite, the SE_A values are higher than the SE_R values in the frequency range 2–18 GHz (Fig. 7b). The result demonstrates that the addition of Ti₃C₂T_x layered particles in the Al has obviously improved the SE_A but decrease the SE_R as compared with pure Al. Ti₃C₂T_x has excellent EMI shielding performance, because its multi-layered structure induces the multiple reflection and scattering of electromagnetic waves, and its high electrical conductivity results in ohmic losses, dielectric polarization, and electric polarization and relaxation. The above mechanisms all contribute to the absorption loss and attenuate the energy of electromagnetic waves [4, 30, 32]. Therefore, the absorption loss is the predominant mechanism in the electromagnetic interference shielding of Ti₃C₂T_x/Al composite.

It should be noted that the EMI SE of 3 wt% Ti₃C₂T_x@Ni/Al composite has considerably enhanced as compared with pure Al and 3 wt% Ti₃C₂T_x/Al (Fig. 7c). The SE_A values of 3 wt% Ti₃C₂T_x@Ni/Al are higher than those of other two materials in the whole frequency range. For example, a SE_A value of about 21 dB at 2.24 GHz for 3 wt% Ti₃C₂T_x@Ni/Al is achieved, higher than 15 dB at the same frequency for 3 wt% Ti₃C₂T_x/Al. This result indicates that the magnetic Ni shell contributes the higher SE_A through magnetic loss. In addition, the SE_A values are slightly lower than the SE_R curve at frequencies lower than 13 GHz, as shown in Fig. 7c. This should be caused by the increasing electrical conductivity of Ti₃C₂T_x@Ni particles, due to the fact that the electrical conductivity of Ni (1.43×10^7 S/m) is higher than that of Ti₃C₂T_x ($100\text{--}1.23 \times 10^6$ S/m [33, 34]). The

synergistic effect of SE_A and SE_R contributes the SE_T of 3 wt% $Ti_3C_2T_x@Ni/Al$.

Figure 7d compares the SE_T curves in the frequency range 2–18 GHz for the three kinds of materials. The commercial EMI shielding requirement is more than 20 dB, ensuring that more than 99% of the incident wave is attenuated. The pure Al and the 3 wt% $Ti_3C_2T_x/Al$ composite have EMI SE values of >20 dB in narrow frequency bands of 1.76 GHz and 3.84 GHz, respectively. The two materials hardly meet the commercial EMI SE requirement. However, the 3 wt% $Ti_3C_2T_x@Ni/Al$ composite has EMI SE values of >20 dB in the frequency ranges of 2–13.4 and 16.4–18 GHz, satisfying the requirement for the commercial EMI shielding applications. In addition, a EMI SE value of 43.8 dB at 2 GHz, nearly 1.7 times those of pure Al and 3 wt% $Ti_3C_2T_x@Ni/Al$, is achieved in the 3 wt% $Ti_3C_2T_x@Ni/Al$ composite (Fig. 7d), enough to block 99.99% of the incident wave.

In the core@shell structured $Ti_3C_2T_x@Ni$ particles, the conductive and multi-layered $Ti_3C_2T_x$ particles but without magnetic mainly contribute to the absorption loss in the electromagnetic interference shielding. However, the Ni shell has high magnetic permeability, enhancing the ability to absorb the energy of electromagnetic waves by the magnetic loss. It has been reported that magnetic particles such as Ni, Co and Fe_3C embedded in composites could enhance the EMI shielding behavior [35–38]. In addition, as the incident waves pass through the multi-layered $Ti_3C_2T_x@Ni$ particles, an alternating magnetic field will produce the eddy-current to dissipate the microwave energy, contributing to the absorption loss. Therefore, the enhanced EMI shielding performance of 3 wt% $Ti_3C_2T_x/Al$ composite should be ascribed to the synergistic effect of the absorption loss of the $Ti_3C_2T_x$ core and the magnetic loss of the Ni shell.

Conclusions

In the present study, Al matrix composites reinforced with core@shell structured $Ti_3C_2T_x@Ni$ particles have been prepared by pressureless-sintering at 650 °C and then hot-extrusion at 450 °C. The mechanical properties and EMI shielding performance were investigated. The main conclusions are summarized as follows:

- (1) Multi-layered $Ti_3C_2T_x$ particles were electroless-plated with Ni, forming a core@shell structure in which the $Ti_3C_2T_x$ layer as a core and the Ni layer as a shell.
- (2) The dense $Ti_3C_2T_x@Ni/Al$ composites demonstrated the improved hardness and tensile strength but the maintained plasticity, resulting from the contributions of the homogeneous distribution of $Ti_3C_2T_x@Ni$, the effective stress transfer from the soft Al matrix to $Ti_3C_2T_x@Ni$, and the multi-absorbing energy mechanisms: delamination, buckling and kinking of $Ti_3C_2T_x$ particles, crack branching and crack deflection.
- (3) $Ti_3C_2T_x@Ni/Al$ composites have an enhanced EMI SE performance, due to the synergistic effect of the absorption loss of the $Ti_3C_2T_x$ core and the magnetic loss of the Ni shell.

Acknowledgement

This work was supported by the National Natural Science Foundation of China under Grant no. 51772020 and Beijing Government Funds for the Constructive Project of Central Universities.

Declaration

Conflict of interest The authors declare that they have no conflict of interest.

References

- [1] Naguib M, Kurtoglu M, Presser V, Lu J, Niu J, Heon M, Hultman L, Gogotsi Y, Barsoum MW (2011) Two-dimensional nanocrystals produced by exfoliation of Ti_3AlC_2 . *Adv Mater* 23:4248–4253. <https://doi.org/10.1002/adma.201102306>
- [2] Naguib M, Mochalin VN, Barsoum MW, Gogotsi Y (2014) MXenes: a new family of two-dimensional materials. *Adv Mater* 26:992–1005. <https://doi.org/10.1002/adma.201304138>
- [3] Anasori B, Lukatskaya MR, Gogotsi Y (2017) 2D metal carbides and nitrides (MXenes) for energy storage. *Nat. Rev. Mater.* 2:1–17. <https://doi.org/10.1038/natrevmats.2016.98>
- [4] Hu SJ, Li SB, Xu WM, Zhang J, Zhou Y, Cheng ZX (2019) Rapid preparation, thermal stability and electromagnetic interference shielding properties of two-dimensional Ti_3C_2

- MXene. *Ceram Int* 45:19902–19909. <https://doi.org/10.1016/j.ceramint.2019.06.246>
- [5] Zhang Y, Wang L, Zhang N, Zhou Z (2018) Adsorptive environmental applications of MXene nanomaterials: a review. *RSC Adv* 8:19895–19905. <https://doi.org/10.1039/C8RA03077D>
- [6] Rosenkranz A, Grützmacher PG, Espinoza R, Fuenzalida VM, Zhang Z (2019) Multi-layer $Ti_3C_2T_x$ -nanoparticles (MXenes) as solid lubricants-role of surface terminations and intercalated water. *Appl Surf Sci* 494:13–21. <https://doi.org/10.1016/j.apsusc.2019.07.171>
- [7] Sliozberg Y, Andzelm J, Hatter CB, Anasori B, Gogotsi Y, Hall A (2020) Interface binding and mechanical properties of MXene-epoxy nanocomposites. *Comp Sci Techn* 192:108124. <https://doi.org/10.1016/j.compscitech.2020.108124>
- [8] Jimmy J, Kandasubramanian B (2020) Mxene functionalized polymer composites: synthesis and applications. *Euro Poly J* 122:109367. <https://doi.org/10.1016/j.eurpolymj.2019.109367>
- [9] Hu J, Li SB, Zhang J, Chang QY, Yu WB, Zhou Y (2020) Mechanical properties and frictional resistance of Al composites reinforced with $Ti_3C_2T_x$ MXene. *Chin Chem Lett* 31:996–999. <https://doi.org/10.1016/j.ccllet.2019.09.004>
- [10] Si XY, Chen FY, Deng QH, Du SY, Huang Q (2018) Preparation and property of MXene/copper alloy composites. *J. Inorg. Mater* 33:603–608. <https://doi.org/10.15541/jim20170297>
- [11] Guo J, Legum B, Anasori B, Wang K, Lelyukh P, Gogotsi Y, Randall CA (2018) Cold sintered ceramic nanocomposites of 2D MXene and zinc oxide. *Adv Mater* 30:1801846. <https://doi.org/10.1002/adma.201801846>
- [12] Fei M, Lin R, Lu Y, Zhang X, Bian R, Cheng J, Luo P, Xu C, Cai D (2017) MXene-reinforced alumina ceramic composites. *Ceram Int* 43:17206–17210. <https://doi.org/10.1016/j.ceramint.2017.08.202>
- [13] Bartolucci SF, Paras J, Rafiee MA, Rafiee J, Lee S, Kapoor D, Koratkar N (2011) Graphene-aluminum nanocomposites. *Mater Sci Eng A* 528:7933–7937. <https://doi.org/10.1016/j.msea.2011.07.043>
- [14] Kwon H, Estili M, Takagi K, Miyazaki T, Kawasaki A (2009) Combination of hot extrusion and spark plasma sintering for producing carbon nanotube reinforced aluminum matrix composites. *Carbon* 47:570–577. <https://doi.org/10.1016/j.carbon.2008.10.041>
- [15] Ma X, Li Y, Hussain I, Shen R, Yang G, Zhang K (2020) Core-shell structured nanoenergetic materials: preparation and fundamental properties. *Adv Mater* 32:2001291. <https://doi.org/10.1002/adma.202001291>
- [16] Cheng J, Wang J, Yun Y, Rui J, Zhao W, Li F (2019) A novel core-shell structure reinforced Zr-based metallic glass composite with combined high strength and good tensile ductility. *J Alloys Compd* 803:413–416. <https://doi.org/10.1016/j.jallcom.2019.06.310>
- [17] Lu W, Guo X, Luo Y, Li Q, Zhu R, Pang H (2019) Core-shell materials for advanced batteries. *Chem Eng J* 355:208–237. <https://doi.org/10.1016/j.cej.2018.08.132>
- [18] Chaudhuri RG, Paria S (2012) Core/shell nanoparticles: classes, properties, synthesis mechanisms, characterization, and applications. *Chem Rev* 112:2373–2433. <https://doi.org/10.1021/cr100449n>
- [19] Chen TJ, Qin H, Zhang XZ (2018) Effects of reheating duration on the microstructure and tensile properties of in situ core-shell-structured particle-reinforced A356 composites fabricated via powder thixoforming. *J Mater Sci* 53:2576–2593. <https://doi.org/10.1007/s40195-014-0159-7>
- [20] Wang Y, Song M, Ni S, Xue Y (2014) In situ formed core-shell structured particle reinforced aluminum matrix composites. *Mater Des* 56:405–408. <https://doi.org/10.1016/j.matdes.2013.11.030>
- [21] Wu W, Guo B, Xue Y, Shen R, Ni S, Song M (2015) Ni-AlxNiy core-shell structured particle reinforced Al-based composites fabricated by in-situ powder metallurgy technique. *Mater Chem Phys* 160:352–358. <https://doi.org/10.1016/j.matchemphys.2015.04.051>
- [22] Zhang JY, Chen TJ, Zhang XZ, Gao M, Geng LB (2020) Simultaneously strengthening and toughening a core-shell structured particulate reinforced aluminum alloy-based composite by solid solution treatment. *J Alloys Compd* 842:155765. <https://doi.org/10.1016/j.jallcom.2020.155765>
- [23] Guo B, Ni S, Shen R, Song M (2015) Fabrication of $Ti-Al_3Ti$ core-shell structured particle reinforced Al based composite with promising mechanical properties. *Mater Sci Eng A* 639:269–273. <https://doi.org/10.1016/j.msea.2015.05.015>
- [24] Zhang J, Li SB, Hu SJ, Zhou Y (2018) Chemical stability of Ti_3C_2 MXene with Al in the temperature range 500–700 °C. *Mater* 11:1979. <https://doi.org/10.3390/ma11101979>
- [25] Zhang J, Kong N, Uzun S, Levitt A et al (2020) Scalable manufacturing of free-standing, strong $Ti_3C_2T_x$ MXene films with outstanding conductivity. *Adv Mater* 32:2001093. <https://doi.org/10.1002/adma.202001093>
- [26] Pramanik S, Koppoju S, Anupama AV, Sahooc B, Suwas S (2018) Strengthening mechanisms in Fe-Al based ferritic low-density steels. *Mater Sci Eng A* 712:574–584. <https://doi.org/10.1016/j.msea.2017.10.056>
- [27] Li SB, Cheng LF, Zhang LT (2002) Identification of damage tolerance of Ti_3SiC_2 by hardness indentations and single edge notched beam test. *Mater Sci Techn* 18:231–233. <https://doi.org/10.1179/026708301225000653>

- [28] Zhang ZF, Sun ZM, Zhang H, Hashimoto H (2004) Micro-scale deformation and damage mechanisms of Ti_3SiC_2 crystals induced by indentation. *Adv Eng Mater* 6:980–983. <https://doi.org/10.1002/adem.200400071>
- [29] Barsoum MW, Radovic M (2011) Elastic and mechanical properties of the MAX phases. *Annu Rev Mater Res* 41:195–227. <https://doi.org/10.1146/annurev-matsci-062910-100448>
- [30] Shahzad F, Alhabeab M, Hatter CB, Anasori B, Hong SM, Koo CM, Gogotsi Y (2016) Electromagnetic interference shielding with 2D transition metal carbides (MXenes). *Science* 353:1137–1140. <https://doi.org/10.1126/science.aaf5471>
- [31] Dou Z, Wu G, Huang X, Sun D, Jiang L (2007) Electromagnetic shielding effectiveness of aluminum alloy-fly ash composites. *Compos Part A-Appl S* 38:186–191. <https://doi.org/10.1016/j.compositesa.2006.01.015>
- [32] Iqbal A, Sambyal P, Koo CM (2020) 2D MXenes for electromagnetic shielding: a review. *Adv Funct Mater* 30:2000883. <https://doi.org/10.1002/adfm.202000883>
- [33] Zhang J, Kong N, Uzun S et al (2020) Scalable manufacturing of free-standing, strong $Ti_3C_2T_x$ MXene films with outstanding conductivity. *Adv Mater* 32:2001093. <https://doi.org/10.1002/adma.202001093>
- [34] Shahzad F, Iqbal A, Kim H, Koo CM (2020) 2D Transition metal carbides (MXenes): applications as an electrically conducting material. *Adv Mater* 32:2002159. <https://doi.org/10.1002/adma.202002159>
- [35] Choudhary HK, Kumar R, Pawar SP, Sundararaj U, Sahoo B (2021) Superiority of graphite coated metallic-nanoparticles over graphite coated insulating-nanoparticles for enhancing EMI shielding. *New J Chem* 45:4592–4600. <https://doi.org/10.1039/D0NJ06231F>
- [36] Choudhary HK, Kumar R, Pawar SP, Sahoo B (2021) Role of graphitization-controlled conductivity in enhancing absorption dominated EMI shielding behavior of pyrolysis-derived $Fe_3C@C$ -PVDF nanocomposites. *Mate Chem Phys* 263:124429. <https://doi.org/10.1016/j.matchemphys.2021.124429>
- [37] Choudhary HK, Kumar R, Pawar SP, Sundararaj U, Sahoo B (2020) Effect of morphology and role of conductivity of embedded metallic nanoparticles on electromagnetic interference shielding of PVDF carbonaceous-nanofiller composites. *Carbon* 164:357–368. <https://doi.org/10.1016/j.carbon.2020.04.007>
- [38] Choudhary HK, Kumar R, Pawar SP, Sundararaj U, Sahoo B (2019) Enhancing absorption dominated microwave shielding in $Co@CePVDF$ nanocomposites through improved magnetization and graphitization of the $Co@C$ -nanoparticles. *Phys Chem Chem Phys* 21:15595–15608. <https://doi.org/10.1039/c9cp03305j>

Publisher's Note Springer Nature remains neutral with regard to jurisdictional claims in published maps and institutional affiliations.